

Global Biogeochemical Cycles®

RESEARCH ARTICLE

10.1029/2024GB008346

A New Framework for the Attribution of Air-Sea CO₂ Exchange

Takamitsu Ito¹  and Christopher T. Reinhard¹ 

¹School of Earth and Atmospheric Sciences, Georgia Institute of Technology, Atlanta, GA, USA

Key Points:

- A time-dependent approach for the mechanistic attribution of air-sea CO₂ exchange is developed based on a linear ordinary differential equation
- The new framework is explained using a stochastic box model and evaluated through an eddy-resolving ocean carbon cycle model
- Application to natural and human-induced processes can aid quantification of the factors controlling ocean-atmosphere carbon exchange

Correspondence to:

T. Ito and C. T. Reinhard,
taka.ito@eas.gatech.edu;
chris.reinhard@eas.gatech.edu

Citation:

Ito, T., & Reinhard, C. T. (2025). A new framework for the attribution of air-sea CO₂ exchange. *Global Biogeochemical Cycles*, 39, e2024GB008346. <https://doi.org/10.1029/2024GB008346>

Received 29 AUG 2024

Accepted 10 JAN 2025

Abstract The air-sea transfer of carbon dioxide can be viewed as a dynamic system through which atmospheric and oceanic processes push surface waters away from thermodynamic equilibrium, while diffusive gas transfer pulls them back toward local equilibrium. These push/pull processes drive significant sub-seasonal, seasonal, and interannual variability in air-sea carbon fluxes, the quantification of which is critical both for diagnosing the ocean response to fossil fuel emissions and for attempts to mitigate anthropogenic climate disruption through intentional modification of surface ocean biogeochemistry. In this study, we present a new approach for attributing air-sea carbon fluxes to specific mechanisms. The new framework is first applied to a two-box ocean nutrient and carbon cycle model as an illustrative example. Next, outputs from a regional eddy-resolving model of the Southern Ocean are analyzed. The roles of multiple physical and biogeochemical processes are identified. The decomposition of the seasonal air-sea carbon flux shows the dominant role of biological carbon pumps that are partially compensated by the transport convergence. Finally, the framework is used to diagnose the response to mesoscale iron and alkalinity release, explicitly quantifying transport feedback and eventual impacts on net air-sea carbon flux. Ocean carbon transport has divergent influences between iron and alkalinity release, due to opposing near-surface gradients of dissolved inorganic carbon. We suggest that our attribution framework may be a useful analytical technique for monitoring natural ocean carbon fluxes and quantifying the impacts of human intervention on the ocean carbon cycle.

Plain Language Summary Significant amounts of carbon dioxide are naturally exchanged between the surface oceans and the atmosphere. Predicting the behavior of the ocean carbon cycle in the coming decades requires that we quantify and understand the effects of physical, biological, and human-induced drivers of ocean-atmosphere carbon exchange. In this study, a new diagnostic framework is developed to explain the individual contributions of multiple physical, biological, and anthropogenic processes to carbon dioxide exchange. We first illustrate this method using a very simple representation of the ocean carbon cycle. Then, we apply the framework to a more realistic three-dimensional simulation of the Southern Ocean, which is rigorously validated with observed carbon dioxide exchange rates. Finally, we simulate a series of human interventions on ocean-atmosphere carbon exchange that modify surface ocean chemistry to foster greater carbon dioxide uptake. Through a computational experiment adding iron or alkalinity to the surface ocean. The techniques developed in this paper can be used across a broad range of natural and human-induced processes to estimate the responses of ocean-atmosphere carbon exchange.

1. Introduction

The oceans are a major sink for atmospheric carbon dioxide (CO₂), absorbing ~3 petagrams of carbon (PgC; 10¹⁵ g) each year (Friedlingstein et al., 2022; Gruber et al., 2023). This uptake of CO₂ by the surface oceans plays a significant role in moderating the impacts of anthropogenic greenhouse gas emissions, with the oceans having taken up as much as 30% of the carbon released by human activities since the start of the industrial period (Gruber et al., 2019). However, anthropogenic carbon uptake is only one of many seasonally and regionally varying carbon fluxes that generally have much larger amplitudes. For instance, during summer, a warming-induced decline in solubility increases the partial pressure of CO₂, leading to outgassing from surface waters (Cai et al., 2020; Takahashi et al., 1993, 2002; Wang et al., 2006). The biological carbon pump tends to oppose seasonal solubility changes, whereby increased biological productivity during summer months tends to lower the partial pressure of CO₂ in surface waters (Fassbender et al., 2018; Takahashi et al., 1993, 2002), fostering CO₂ uptake into the surface ocean. Deconvolving the key factors controlling variation in air-sea CO₂ flux is thus

critical for diagnosing anthropogenic impacts on the ocean carbon cycle (McKinley et al., 2017) and for predicting the ocean response to environmental change across a range of timescales.

There is also significant ongoing interest in intentionally modifying surface ocean biogeochemistry to enhance the uptake and/or storage of CO₂ from the atmosphere as a component of climate mitigation portfolios. For example, significant venture funding is currently being channeled into ocean-based carbon dioxide removal (CDR) startups (Lebling et al., 2022) and the U.S. National Academies of Science, Engineering, and Medicine (NASEM) recently recommended \$2.5 billion in research funding on ocean-based CDR approaches over the next decade (National Academies of Sciences, 2021). However, applying any of these approaches at scale will require robust frameworks for monitoring and attributing carbon fluxes across a wide range of spatial and temporal scales against a complex and time-varying natural background. As a result, there is strong impetus to develop new technologies and analytical frameworks aimed at quantitatively evaluating specific contributors to ocean uptake of CO₂ from the atmosphere that can become core components of monitoring, reporting, and verification (MRV) of ocean-based carbon dioxide removal (CDR).

There are two complementary approaches to quantify the drivers of air-sea CO₂ exchange, namely *p*CO₂-based and mass-balance-based approaches. First, the *p*CO₂-based approach focuses on the surface ocean partial pressure of CO₂ (*p*CO₂) as the primary factor controlling the air-sea CO₂ exchange (e.g., Ayers & Lozier, 2012; Lovenduski et al., 2007; Sarmiento & Gruber, 2006; Takahashi et al., 2002). The *p*CO₂-based approach uses the carbonate chemistry to attribute observed *p*CO₂ changes to the four factors including temperature (*T*), salinity (*S*), alkalinity (*A*) and dissolved inorganic carbon (*C*). Takahashi et al. (2002) first demonstrated the explanatory power of the co-located *p*CO₂ and *T* observations in explaining the seasonal cycle of surface *p*CO₂ due to temperature-driven (solubility) and non-thermal (biological) components. In subtropical oceans, seasonal warming and cooling dominate the corresponding seasonal change of *p*CO₂. At subpolar latitudes, the seasonal phasing of *p*CO₂ is generally opposite of the temperature-driven change, indicating the important role of non-thermal mechanisms. Ayers and Lozier (2012, hereafter AL12) further developed this approach to include additional contributions from salinity, dissolved inorganic carbon, and alkalinity to diagnose the drivers of surface ocean *p*CO₂ tendencies in the North Pacific Ocean.

Second, the mass-balance-based approach utilizes the carbon mass balance of the surface ocean (e.g., Follows & Williams, 2004; Lauderdale et al., 2016). The input/output of carbon in the surface ocean must be balanced between air-sea CO₂ exchange, ocean transport and biological processes at the steady state. While it is difficult to accurately estimate the carbon mass balance based on the observation alone, it is possible to use outputs from computational carbon cycle models that are validated with observational data. Lauderdale et al. (2016, hereafter L16) developed a mass-balance based theory to quantitatively attribute the air-sea exchange of CO₂ to several driving mechanisms such as physical transport, biological carbon uptake, and surface buoyancy fluxes under the assumption of steady state mean seasonal cycles. The mass balance approach is particularly suitable for understanding model output as the computational models strictly follow the carbon mass balance.

Both AL12 and L16's approaches are based on the seasonal and annual mean climatology of CO₂ fluxes. Though both studies successfully showed the decomposition of air-sea CO₂ flux drivers, these approaches face some limitations. First, these frameworks are built on statistical mean states where sub-seasonal to interannual variability of carbon are neglected. This limits the applicability of these approaches to ocean-based CDR, which requires the attribution of time-dependent air-sea CO₂ exchanges. Second, these and other previous frameworks do not include the negative feedback of diffusive gas transfer. For example, a sudden removal of carbon from the equilibrated surface ocean can induce an undersaturated surface *p*CO₂, driving air-to-sea CO₂ transfer. The addition of CO₂ will re-equilibrate the surface ocean over time, and this establishes a stabilizing feedback. Air-sea CO₂ equilibration timescales vary from several months to a year depending on background atmospheric and oceanographic conditions (Broecker & Peng, 1974; Jones et al., 2014). This negative feedback should thus play a key role in shaping the spatial and temporal patterns of air-sea CO₂ fluxes.

In this study, we present a novel framework for quantifying the drivers of air-sea CO₂ exchange that explains the time-dependent drivers of air-sea CO₂ exchange by combining the *p*CO₂ and mass balance-based approaches. The conceptual core of our framework is to represent air-sea exchange of CO₂ with a linear ordinary differential equation (ODE) (Di Lorenzo & Ohman, 2013; Hasselmann, 1976; Yuan et al., 2004), which is derived from the governing equations of the ocean carbon cycle, including carbonate chemistry and reactive transport of carbon. In typical oceanographic conditions, the air-sea exchange of CO₂ is not a dominant term of the surface ocean carbon

mass balance at subseasonal to seasonal timescales but is rather a relatively small residual between transport divergence, local storage and biological carbon uptake. Changes in local storage ($\partial C/\partial t$ in carbon mass balance), which is neglected in the AL12 and L16 theory due to the steady state assumption, play a crucial role in the negative feedback that regulates air-sea CO₂ exchange. This time-dependent term is retained in our theory through the transformation of the governing equations to an linear ODE model. Specifically, we can combine the time derivative of air-sea gas exchange with constraints from the carbonic acid system and the time-varying carbon budget including the negative gas exchange feedback to arrive at an expression that governs the time-dependent evolution of CO₂ exchange. A detailed derivation of this framework is presented in Section 2.

In what follows, we outline the theoretical derivation of the linear ODE (Section 2). Then, we illustrate the new framework through a stochastically forced 2-box ocean nutrient and carbon cycle model (Section 3), and provide a computational example that can be run on a personal computer. We then present a realistic example using a regional eddy-resolving carbon cycle model (Section 4), and illustrate the sequence of events following meso-scale iron and alkalinity release experiments in the Southern Ocean (Section 5). Finally, we discuss the implications of our results and possible future applications of our framework (Section 6).

2. Theory

The underlying principles of the linear ODE come from three equations governing the surface mass balance of dissolved inorganic carbon (Equation 1), surface water carbonate chemistry (Equation 2), and the parameterization of air-sea gas transfer (Equation 3):

$$\frac{\partial C}{\partial t} = -\nabla \cdot \mathbf{u}C + \nabla \cdot \mathbf{K}\nabla C - B + \frac{C}{h}(E - P) + \frac{F}{h}, \quad (1)$$

$$[\text{CO}_2] = \alpha(T, S, A, C), \quad (2)$$

$$F = G(1 - f_{\text{ice}})(K_H p\text{CO}_2^{\text{atm}} - [\text{CO}_2]), \quad (3)$$

where C is the concentration of dissolved inorganic carbon, \mathbf{u} is the three-dimensional velocity vector, and \mathbf{K} is the turbulent diffusivity tensor. B is the net carbon sink due to the biological pump, and h is the thickness of the surface layer, which we set here at 50 m. $E-P$ is evaporation minus precipitation, and F represents the air-sea flux of CO₂ from the atmosphere (e.g., positive values denote a CO₂ flux from the atmosphere into the ocean).

The concentration of dissolved carbon dioxide [CO₂] is a function of temperature (T), salinity (S), alkalinity (A), and dissolved inorganic carbon (C), and the detailed functional form of α is determined by the equilibrium carbonate chemistry. G is the gas transfer coefficient and is a function of the 10-m wind speed and the Schmidt number for CO₂ (Wanninkhof, 2014). Fractional ice cover (f_{ice}) also modulates the area-integrated the rate of gas exchange. K_H is the Henry's law coefficient for the solubility of CO₂, which is a function of temperature and salinity. $p\text{CO}_2^{\text{atm}}$ is the partial pressure of carbon dioxide in the overlying atmosphere, while [CO₂] is the concentration of carbon dioxide in seawater. Here, we combine these two factors to define $G^* = G(1 - f_{\text{ice}})$.

Taking the time derivative of the carbonate chemistry (Equation 2) reveals mechanistic linkages between carbon dioxide and variability of T , S , A , and C , which has been previously applied in the North Pacific basin through the AL12 theory. A detailed derivation of the theory is provided in Appendix A. Building on this approach, time derivatives of Equations 2 and 3 can be combined to eliminate the tendency of [CO₂] and to establish the linkage between the rate of change in air-sea CO₂ transfer and the rate of change in T , S , A , and C along with other variables. Then, Equation 1 can be used to eliminate the rate of change in C . The resulting equation can then be rewritten using air-sea CO₂ exchange, F , as the prognostic variable.

$$\begin{aligned} \frac{\partial F}{\partial t} = & -\frac{G^* \alpha_C}{h} F + \left[G^* \alpha_C \nabla \cdot (\mathbf{u}C) \right. \\ & - G^* \alpha_C \nabla \cdot (\mathbf{K}VC) \\ & + G^* \alpha_C B \\ & - G^* \alpha_A \dot{A} \\ & \left. - G^* \left\{ \frac{\alpha_C C}{h} (E - P) + \alpha_S \dot{S} \right\} \right], \quad (4) \\ & + G^* \{ K_{HP} \text{CO}_2^{\text{atm}} - \alpha_T \dot{T} \} \\ & + G^* K_{HP} \dot{\text{CO}}_2^{\text{atm}} \\ & + G^* \{ K_{HP} \text{CO}_2^{\text{atm}} - [\text{CO}_2] \} \end{aligned}$$

where a local time derivative is expressed as a dot above the variable ($\dot{\chi} \equiv \partial \chi / \partial t$) and the partial derivatives of α values are expressed as subscripts ($\alpha_\chi \equiv \partial \alpha / \partial \chi$). It can be seen that this formulation takes the form of a first-order linear differential equation, which can be re-written as follows:

$$\frac{\partial F}{\partial t} = -\lambda F + \sum_n f_n. \quad (5)$$

Similar differential equations have been used for calculating perturbations to the marine carbon cycle as pulse-response functions (Hooss et al., 2001; Joos & Bruno, 1996; Yankovsky et al., 2024) in order to model the impacts of anthropogenic perturbations and interventions. Our new framework can diagnose the responses of air-sea CO₂ flux to a range of physical and biogeochemical drivers for both natural and anthropogenic processes. In the RHS of Equation 5, f_n denotes the forcing terms from individual physical and biogeochemical processes that control air-sea CO₂ fluxes (e.g., advection, mixing, biological uptake, temperature shifts, and atmospheric transients as mathematically defined in the RHS of Equation 4). These forcing terms collectively define the temporal evolution of F , the air-sea CO₂ flux. The strength of the negative air-sea flux feedback is measured by the magnitude of the λ coefficient in the first term on the RHS of Equation 5, and has the units of inverse time:

$$\lambda = \frac{G^* \alpha_C}{h}. \quad (6)$$

The mechanisms revealed in the form of Equation 4 illustrate the dynamics governing the evolution of air-sea CO₂ transfer. In particular, Equation 4 suggests that diffusive gas exchange tends to bring the surface water toward air-sea equilibrium ($F = 0$) on an exponential decay timescale of λ^{-1} , while the suite of physical and biogeochemical processes (represented as f_n terms in Equation 5) act to push surface waters away from equilibrium. A larger value of λ denotes stronger negative feedback, where diffusive gas exchange drives more rapid air-sea equilibration. On the RHS of Equation 4, we group the forcing terms into eight representative components, including (a) advection of C , (b) turbulent mixing of C , (c) carbon uptake by the biological pump, (d) changes in alkalinity, (e) evaporation minus precipitation, (f) changes in solubility, (g) changes to atmospheric CO₂, and (h) changes in the air-sea gas exchange coefficient (including the effect of partial sea ice cover). Most of these factors are accounted for by the L16 theory, in that the steady-state approximation of Equation 4 is essentially identical to the L16 attribution framework after replacing C by the sum of the saturation and residual components. In practice, some forcing terms (f_n) in Equation 4 may be determined from observations or models (such as temperature shifts and atmospheric transients), while others may be difficult to determine accurately based on the observations only and will likely require numerical models (such as advection and mixing of carbon). If the detailed structure of the forcing terms (f_n) is known, they can be individually integrated to determine the quantitative contribution of each term to the overall air-sea CO₂ exchange flux:

$$\frac{\partial F_n}{\partial t} = -\lambda F_n + f_n, \quad (7)$$

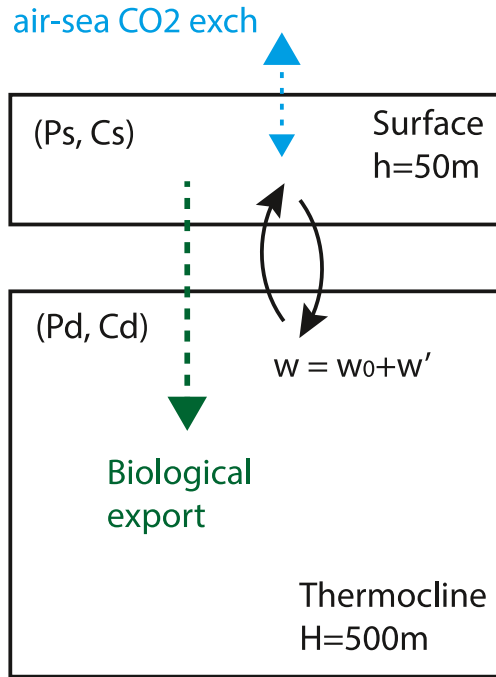


Figure 1. A schematic diagram of the 2-box model is discussed in the text. The model includes phosphorus (P) and dissolved inorganic carbon (C). The subscripts indicate the surface (s) and deep (d) boxes. The model represents vertical transport (black arrows), biological carbon export (green arrow), and air-sea CO₂ exchange (blue arrow). The temperature, salinity, and alkalinity of the surface box are prescribed for simplicity.

$$F = \sum_n F_n. \quad (8)$$

Since this is a linear system, the superposition principle applies to F_n (Equation 8), with the result that Equations 7 and 8 can be used as an analytical framework for quantifying the roles of individual physical and biogeochemical processes (F_n) in regulating the evolution of air-sea carbon dioxide exchange (F) in a time-dependent manner.

3. A Stochastic Box Model

To illustrate the application of our attribution framework (Equations 4–8), we employ a stochastically forced 2-box ocean nutrient and carbon cycle model (Hamme & Emerson, 2002; See Figure 1). The model includes a 50 m-thick ($h = 50$ m) surface ocean and 500 m-thick ($H = 500$ m) thermocline boxes, and includes the tracers phosphorus (P) as a macro-nutrient and dissolved inorganic carbon (C). The random forcing comes from the imposed vertical mixing rate specified in the model via mixing of surface and thermocline boxes with a vertical exchange rate, w , in units of ms^{-1} . The ocean vertical exchange is highly variable due to many physical processes including atmospheric storms, turbulent mixing, breaking internal waves, and ocean mesoscale and sub-mesoscale eddies. To represent the complexity of these processes in a crude way, we use a random noise in the vertical mixing rate (w) where the temporally varying vertical mixing is parameterized as $w(t) = w_0 + w'(t)$. The background mixing rate (w_0) is set to 10^{-6}ms^{-1} . A random Gaussian noise (w') is added with zero-mean and an amplitude of $3 \cdot 10^{-6} \text{ms}^{-1}$, and we enforce that the value of w remains positive or zero to avoid up-gradient mixing of nutrients in the two-box system. We implement stochastic forcing on the vertical exchange rate (w') via the pseudo-random number generator of the numpy library in python.

For simplicity, biological export of organic matter from the surface box is parameterized as a linear function of surface P with an inverse nutrient uptake timescale, λ_{bio} , which is set to 100 days ($\lambda_{\text{bio}} = 1.16 \cdot 10^{-7} \text{s}^{-1}$). The governing equations of P cycling are specified as follows, with organic matter exported from the surface box being fully remineralized in the thermocline box:

$$\frac{\partial P_s}{\partial t} = \frac{w}{h}(P_d - P_s) - \lambda_{\text{bio}}P_s, \quad (9)$$

$$\frac{\partial P_d}{\partial t} = \frac{w}{H}(P_s - P_d) + \frac{\lambda_{\text{bio}}h}{H}P_s. \quad (10)$$

The carbon and phosphorus cycles are coupled through Redfield stoichiometry with a constant C:P ratio of 106 (Redfield et al., 1963; for justification see Hamme and Emerson (2002, Chapter 3). Finally, air-sea CO₂ exchange is parameterized using a simplified diffusive gas exchange formulation with a constant gas transfer coefficient (G) of $2,000 \text{myr}^{-1}$ or equivalently, $6.34 \cdot 10^{-5} \text{ms}^{-1}$:

$$\frac{\partial C_s}{\partial t} = \frac{w}{h}(C_d - C_s) - \lambda_{\text{bio}}R_{C:P}P_s - \frac{GKH}{h}(p\text{CO}_{2,\text{ocn}} - p\text{CO}_{2,\text{atm}}), \quad (11)$$

$$\frac{\partial C_d}{\partial t} = \frac{w}{H}(C_s - C_d) + \frac{\lambda_{\text{bio}}hR_{C:P}}{H}P_s. \quad (12)$$

For the calculation of carbonate chemistry, we assume a constant surface salinity of 35 psu and carbonate alkalinity of $2,200 \mu\text{eq kg}^{-1}$ and use the PyCO2SYS package to calculate the carbonate chemistry coefficients and

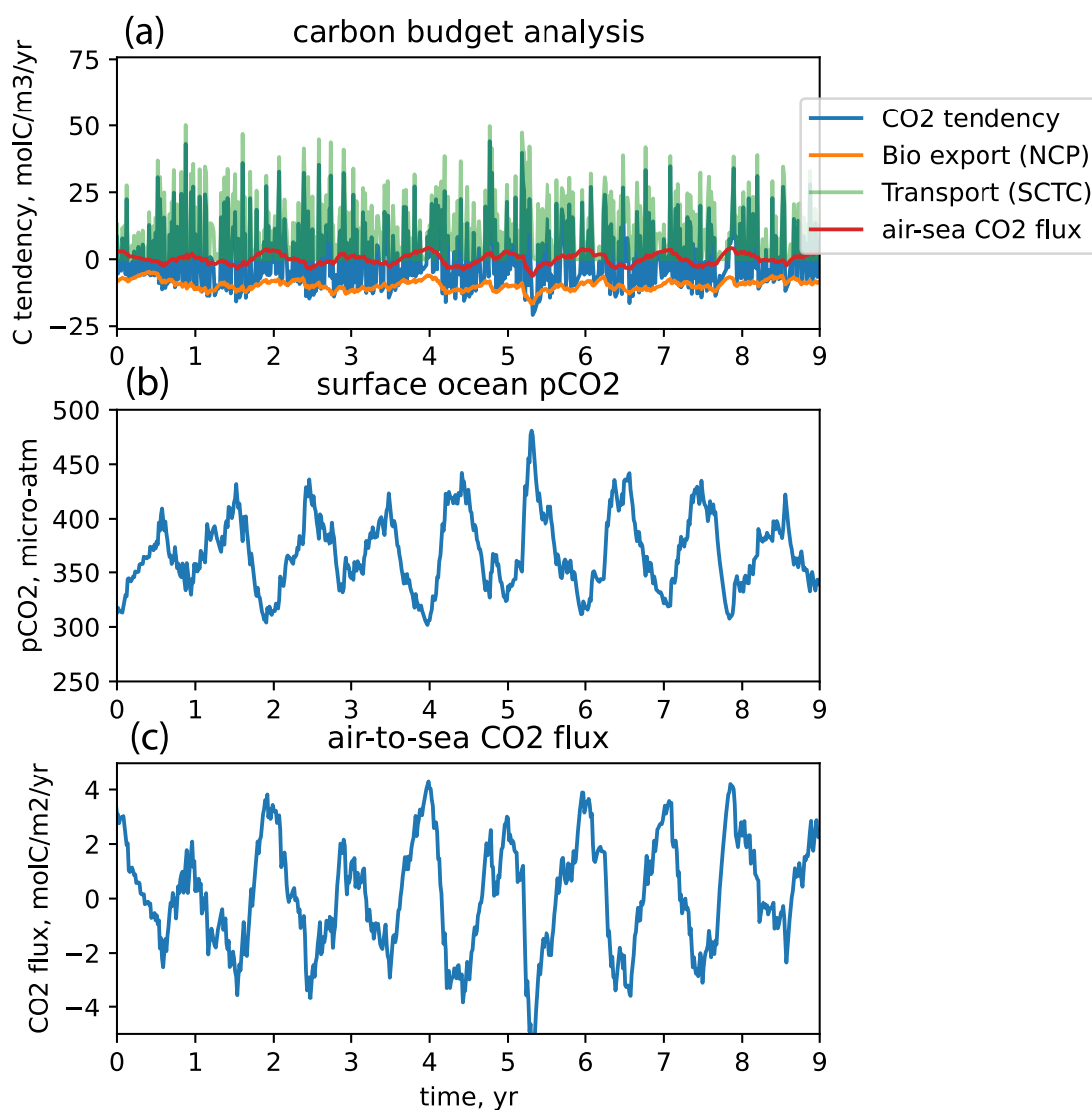


Figure 2. Model output for 9 years of a 2-box model simulation. (a) Top panel shows the carbon budget terms in the surface box in the units of $\text{molC m}^{-3} \text{ year}^{-1}$. The blue line shows local storage (CO_2 tendency; dC/dt), the orange line shows biological export ($\text{NCP} = \text{Net Community Production}$), the green shows vertical transport ($\text{SCTC} = \text{Surface Carbon Transport Tendency}$), and the red line shows air-sea CO_2 exchange. (b) Surface ocean $p\text{CO}_2$. (c) Air-sea CO_2 flux (same as the red line in (a) but rescaled for visibility).

the derivatives α_T , α_S , α_A , and α_C (Humphreys et al., 2022). Sea surface temperature is prescribed to annual mean temperature of 15°C with a mean seasonal cycle of 3°C amplitude via a cosine function.

The model Equations 9–12 are coded in python and are integrated numerically. The code is hosted at the github repository and can be executed on a cloud server (see the Data Availability Statement). The model is initialized with an arbitrary initial condition of $P_s = 0.5 \mu\text{molPkg}^{-1}$, $P_d = 2.0 \mu\text{molPkg}^{-1}$, $C_s = 1,900 \mu\text{molC kg}^{-1}$, and $C_d = 2,200 \mu\text{molC kg}^{-1}$, and is spun up for 90 years via forward integration with 5-day timestep, which is adequate for this idealized model. Atmospheric $p\text{CO}_2$ ($p\text{CO}_{2,\text{atm}}$) is initially prescribed at 360 ppm, and increases linearly at a rate of 2 ppm-year^{-1} following spin-up. Figure 2 shows the results for the 9-year period in the model simulation.

The prescribed seasonal cycle of surface temperature drives seasonal changes in CO_2 solubility and air-sea CO_2 exchange. The carbon budget of the surface box (Figure 2a) is dominated by the surface carbon transport convergence driven by stochastic vertical mixing, which is primarily balanced by the local carbon storage ($\partial C/\partial t$). On longer timescales (several months and years), the net carbon input due to vertical mixing is balanced

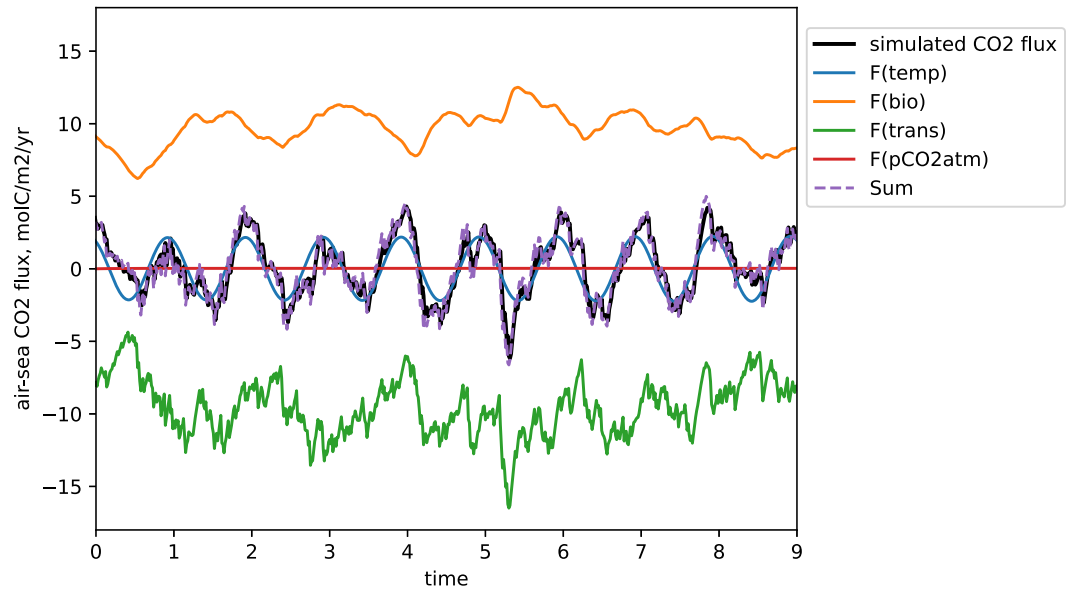


Figure 3. Air-sea CO₂ exchange and its components. The black solid line shows the direct model output for the air-to-sea CO₂ flux, while the purple dashed line is the sum of the four flux components calculated from the individual integration of forcing terms (Equations 13–17). The green line indicates the contribution of the surface carbon flux convergence, and the orange line indicates the contribution from biological carbon export.

by net community production (biological carbon export). Between these terms, the net air-sea CO₂ exchange is a relatively small residual with alternating seasonal uptake and outgassing (Figure 2c). The seasonal pCO₂ and air-sea exchange flux variability are controlled primarily by changes in solubility, while the effect of stochastic transport perturbation is visible in the variability of surface ocean pCO₂ and the air-sea CO₂ exchange rates.

We can transform Equation 11 into the first-order linear differential equation following the steps of Equations 4 and 5 according to

$$\frac{dF}{dt} = -\frac{G\alpha_C}{h}F + \{f_{\text{trans}} + f_{\text{bio}} + f_T + f_{\text{atm}}\}, \quad (13)$$

with the forcing terms on the RHS defined as follows:

$$f_{\text{trans}} = -\frac{G\alpha_C w}{h}(C_d - C_s), \quad (14)$$

$$f_{\text{bio}} = G\alpha_C \lambda_{\text{bio}} R_{C:P} P_s, \quad (15)$$

$$f_T = G \left(p\text{CO}_{2,\text{atm}} \frac{dK_H}{dt} - \alpha_T \frac{dT}{dt} \right), \quad (16)$$

$$f_{\text{atm}} = GK_H \frac{dp\text{CO}_{2,\text{atm}}}{dt}. \quad (17)$$

In this particular integration, there are four forcing terms, and their respective contribution to the air-to-sea CO₂ flux is displayed in Figure 3. First, the surface carbon transport (Equation 14, blue line in Figure 3) is the net input of carbon due to vertical mixing, which leads to a negative air-to-sea flux (degassing). Second, biological carbon export is the primary net sink of carbon (Equation 15, green line in Figure 3), which drives a positive air-to-sea flux (uptake). Both of these terms include a significant stochastic component, and mostly cancel one another. Third, seasonal warming and cooling controls the solubility of CO₂ (Equation 16, gray line in Figure 3), which drives seasonal uptake in the fall due to the transition from the warm, low-solubility season to the cool, high-solubility season. Finally, the atmospheric pCO₂ transient drives a small positive air-to-sea flux

due to the gradually rising atmospheric $p\text{CO}_2$ level (Equation 17, red line in Figure 3). The transient atmospheric CO_2 is included to be more realistic. While this drift in the atmospheric CO_2 violates the equilibrium assumption of the stability analysis, its magnitude is significantly smaller than the stochastic forcing.

Comparing Figure 2a and 3 reveals the explanatory power of the new approach. The upper ocean carbon budget (Figure 2a) is extremely noisy and is dominated by the balance between the transport convergence and local accumulation. This makes it difficult to visually identify the driving factors of the overall air-sea CO_2 exchange flux. In contrast, the new attribution framework (Figure 3) is based on a linear ODE (Equations 7 and 8), in which the air-sea CO_2 flux (F) integrates individual forcing mechanisms (f_n) as a low-pass filter. This effectively filters out high-frequency noise, with the filtering timescale (λ^{-1}) being underpinned by the governing equations and the negative feedback associated with the diffusive gas transfer.

The linear ODE approach assumes that λ is constant and the system is at equilibrium. Under typical oceanographic conditions, we may expect $G \sim 1,500 \text{ m year}^{-1}$, $h \sim 50 \text{ m}$, and $a_c \sim 0.1$, yielding a rough estimate for the exchange time scale (λ^{-1}) of ~ 0.2 years. In the box model, these parameters are simply prescribed. In reality, the magnitudes of G , h , and a_c are not constant but rather vary with local oceanic and meteorological conditions. Within our theory, the variability of G can be treated as a forcing (the last term in the RHS of Equation 4), while the depth h depends on the surface layer thickness. Thus, the strength of the negative feedback and the air-sea equilibration timescale would be expected to vary spatially and temporally depending on detailed regional patterns of G , h , and a_c , while the magnitude of the exchange timescale (λ^{-1}) should be on the order of several months. In the next section, we evaluate the new attribution framework in a more realistic setting using an eddy-resolving regional ocean carbon cycle model.

4. Application in an Eddy-Resolving Regional Ocean Carbon Cycle Model

As a more realistic application, we employ a model hindcast from an eddy-resolving (10 km resolution) model of the central South Pacific sector of the Southern Ocean (Ito, 2022). The model has previously been validated to reproduce climatological patterns and temporal variability of physical and biogeochemical variables, including the partial pressure of CO_2 (Figure 4). Briefly, the model is based on MITgcm (Marshall, Adcroft, et al., 1997; Marshall, Hill, et al., 1997) with a 6-phytoplankton configuration of the Darwin ecosystem model (Dutkiewicz et al., 2014, 2015).

The model domain covers from 164°W to 100°W and 65°S to 44°S and is one-way nested with the Biogeochemical Southern Ocean State Estimate (Verdy & Mazloff, 2017). This regional domain includes the Udintsev Fracture Zone (UFZ) in the central Pacific sector of the Southern Ocean. The UFZ is characterized by the deep gap between the Pacific-Antarctic Ridge and the East Pacific Rise, which is one of the key choke points of the Antarctic Circumpolar Current. The model reproduces observation-based gridded $p\text{CO}_2$ products remarkably well from seasonal to interannual timescales ($r = 0.89$). The model represents an intermittent double-peak pattern of $p\text{CO}_2$, with one peak driven by the summer-time high temperature and another during the winter-time high of dissolved inorganic carbon. A similar pattern was observed in the Drake Passage region based on the SOCAT data set (Jersild & Ito, 2020). The model also captures the spatial and temporal structure of the regional net primary production with respect to the satellite ocean color products, and biogeochemical tracer variability observed by BGC-Argo floats as shown in Ito (2022).

Unlike in the 2-box model, there is significant spatio-temporal variability of G , h , and a_c , making it difficult to directly apply Equation 6 to determine the magnitude of λ for the whole model domain. Alternatively, the timescale (λ^{-1}) can be estimated from the lag-autocorrelation of the air-sea CO_2 flux (F) anomaly. Figure 5 shows the lag-autocorrelation of the de-trended and de-seasoned air-sea CO_2 flux (F) anomaly averaged over the analysis region. Based on the comparison to the exponentially decaying functions, an exchange timescale of approximately 50 days fits this particular model output well, which is also consistent with the observation-based estimates of air-sea CO_2 equilibration timescale for this region (Jones et al., 2014).

A key feature of this formulation is the quantification of contributions from each individual forcing term to the overall ocean CO_2 uptake. We can thus integrate Equation 7 separately for each forcing term (f_n) to yield an estimate of air-sea CO_2 flux associated with each specific mechanism, with the total air-sea carbon flux as the sum of individual integration. Implementing this theoretical framework in the context of numerical model output with sufficient physical resolution and predictive skill provides a flexible mechanistic framework for quantitative

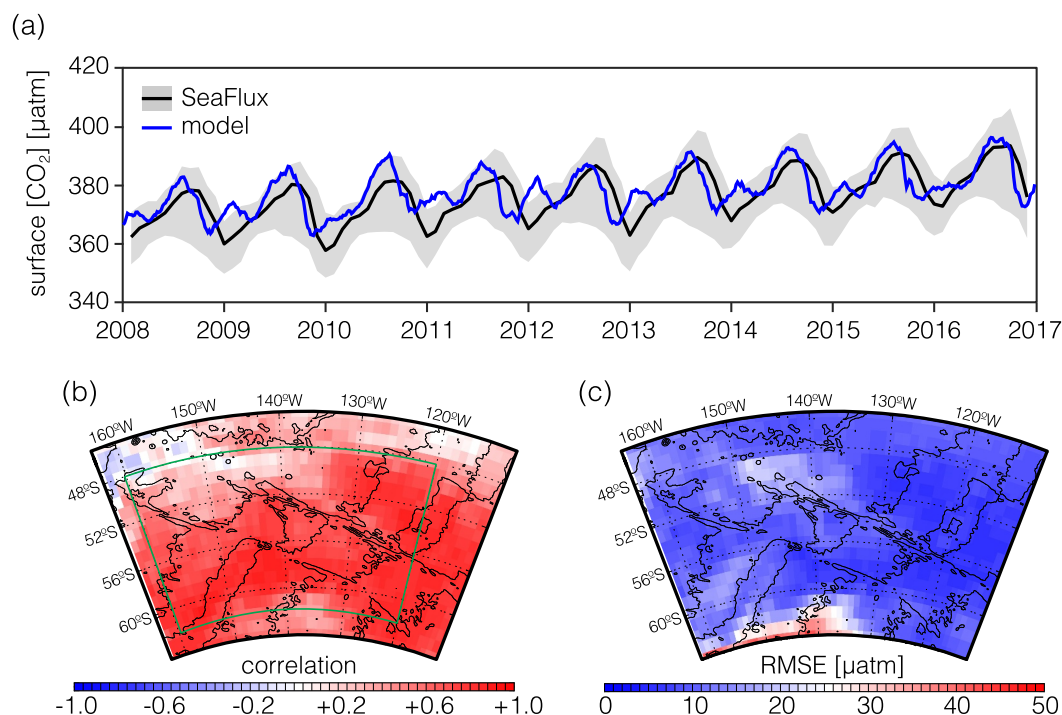


Figure 4. Validation of the regional carbon cycle model. (a) Domain-average surface ocean $p\text{CO}_2$ in the model (blue) and observation-based products (black/gray, Fay et al., 2021). (b) Spatial pattern of temporal correlation coefficient, R . (c) Root-mean-square error (RMSE). For (b) and (c), the model output is interpolated onto $1^\circ \times 1^\circ$ grid before comparing to the observation-based products. The thin black lines represent contours showing bottom topography.

attribution of the mechanisms regulating ocean carbon uptake over time. To assemble f_n terms, the individual terms within the curly bracket in the RHS of Equation 4 can be diagnosed from model output. More specifically, we can integrate each of the RHS terms in Equation 4 over a control volume, which can cover any region of interest from a specific site to an arbitrarily large region. For this particular example, we choose to cover most of the model domain away from the open boundaries covering 160°W – 120°W and 48°S – 62°S as indicated by the teal box in Figure 4b. Vertically, we integrate over the upper 50 m of the water column. Temporally, we use the 5-day average model output over the 8-year period from 2009 to 2016. In this region of the model, biological uptake

represents the major sink of carbon (Figure 6a, green line), and this uptake drives a significant air-sea carbon flux into the regional surface ocean (Figure 6b). The finite timescale of air-sea gas transfer naturally integrates out the high-frequency changes in physical transport and other fluxes, with the resulting time series exhibiting variations on the timescale of λ^{-1} and longer.

We can deconvolve the air-sea CO_2 exchange through the term-wise integration of the linear ODE (Equation 7), integrating through the full seasonal cycle and multi-year trend. Physical transport is split into two components for the advective transport and (parameterized) mixing including the contributions from the KPP mixing parameterization (Large et al., 1994), both of which are highly variable. As in the 2-box model, the linear ODE framework acts as a low-pass filter that transforms rapidly varying transport-driven f_n terms into slowly varying carbon flux components (F_n) with a characteristic timescale λ^{-1} . Averaging over the entire hindcast, our framework diagnoses biological carbon fixation (net community production) as the primary driver of regional air-sea carbon flux (2.4 million tonnes of CO_2 per day = $2.4 \text{ MtCO}_2 \text{ d}^{-1}$), and this is largely compensated by the transport convergence ($-2.1 \text{ MtCO}_2 \text{ d}^{-1}$) and changes to solubility ($-0.07 \text{ MtCO}_2 \text{ d}^{-1}$). While there

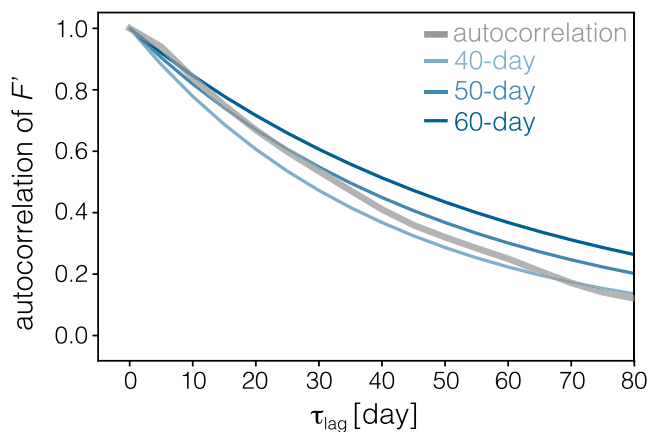


Figure 5. Lag-autocorrelation function of the de-trended and de-seasoned air-sea CO_2 flux anomaly. The thick gray line is based on the model output, which is compared to an exponential function with 40-, 50-, and 60-day timescales.

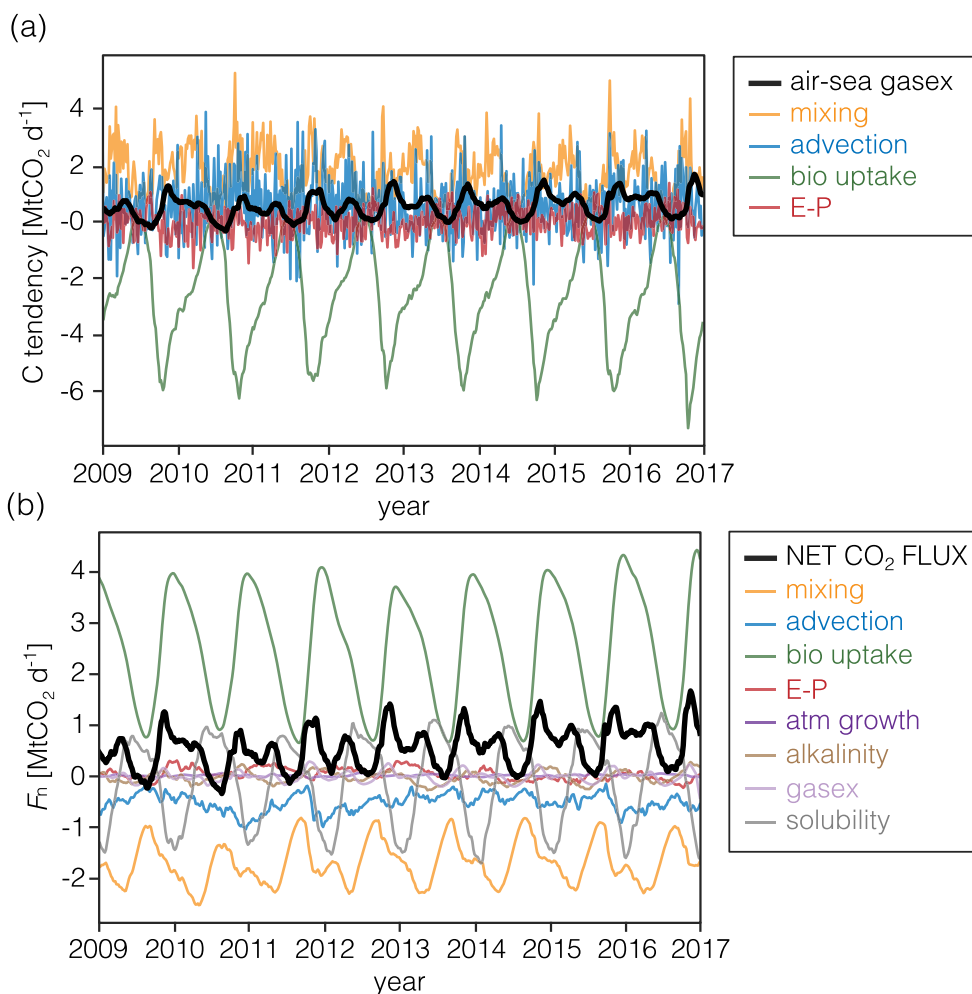


Figure 6. Attribution of ocean carbon uptake in the eddy-resolving ocean carbon cycle model of the Southern Ocean. (a) Time series of surface carbon budget terms as flux convergence over the model domain including air-sea gas exchange, mixing, advection, biological uptake, and evaporation minus precipitation (E-P). (b) Deconvolved surface ocean carbon fluxes using our linear ODE framework, showing flux contributions from mixing, advection, biological uptake, evaporation minus precipitation (E-P), atmospheric growth, alkalinity changes, changes in gas exchange rate, and changes in solubility, along with the net sea-air CO₂ flux (thick black line). Positive values indicate CO₂ uptake by the surface ocean, while negative values indicate CO₂ outgassing. Analysis is performed for the upper 50 m of the model domain covering from 160°W to 120°W and 48°S to 62°S, including the seasonal cycle, long-term trends, and variability.

are several other factors, these three terms dominate the regionally integrated air-sea carbon flux of 0.5 MtCO₂ d⁻¹.

5. Attribution of CO₂ Fluxes During Iron and Alkalinity Addition to the Surface Ocean

Next, we perturb the regional Southern Ocean model by performing two simulations of mesoscale iron and alkalinity release to a patch of the surface ocean with the objective of quantifying the impact of transport feedback on ocean carbon uptake efficiency. The first case is meant to broadly mimic field trials of ocean iron fertilization (OIF), a proposed approach toward sequestering carbon in the ocean interior through stimulation of the biological carbon pump in regions of the ocean in which photosynthetic carbon fixation is limited by available Fe (Boyd et al., 2000; Buesseler et al., 2004). The second case is meant to represent direct addition of alkalinity to the ocean surface (ocean alkalinity enhancement, OAE), for example, through electrochemistry or controlled reactor approaches, which is also being pursued as a potential ocean-based CDR technology (Eisaman, 2020; Ferderer et al., 2022; National Academies of Sciences, 2021; Rau, 2009). Both perturbations lead to changes in the near-surface gradients of DIC, altering the local carbon transport divergence and the air-sea carbon exchange. The

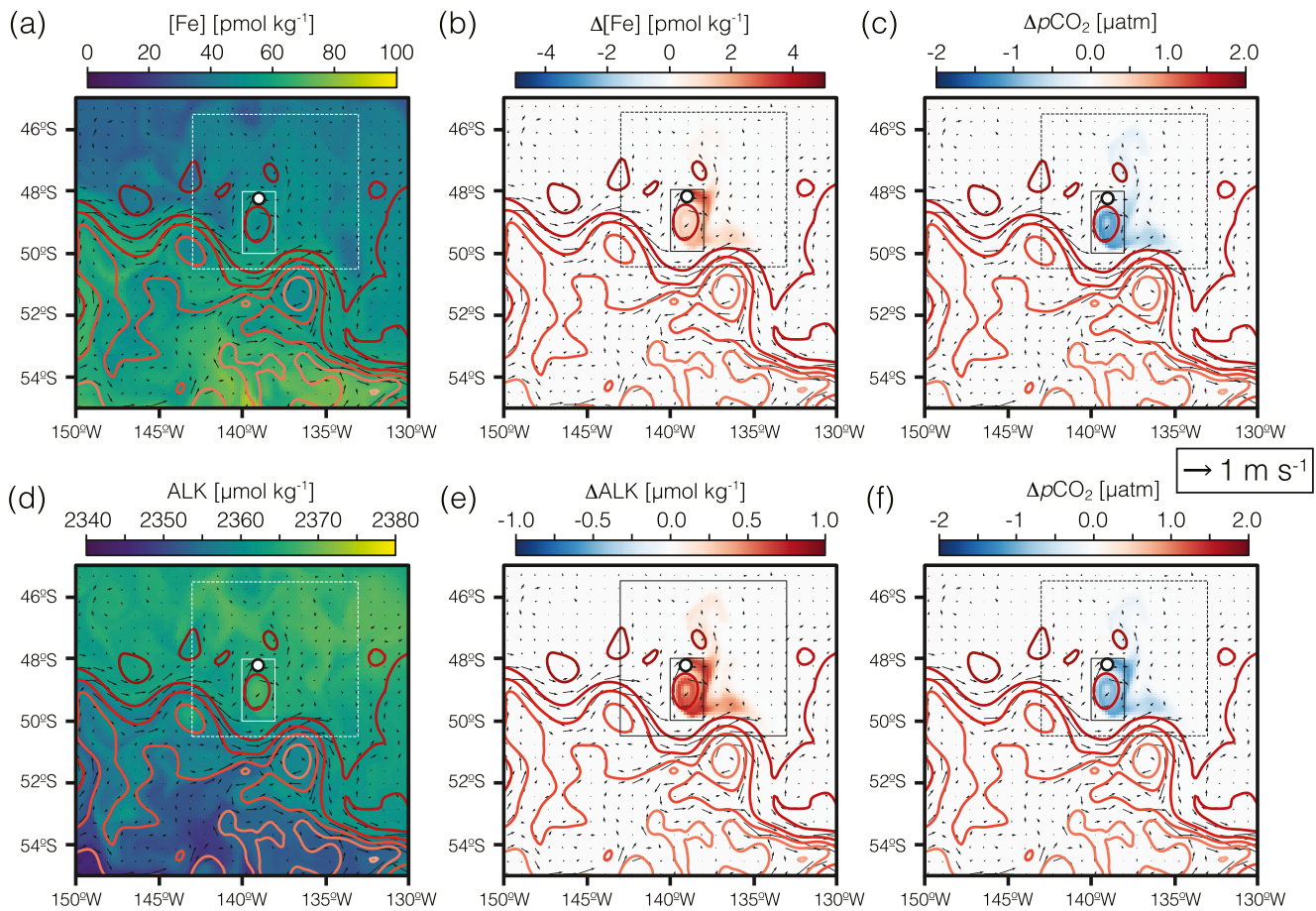


Figure 7. Surface ocean chemistry for mesoscale ocean iron fertilization (OIF; a–c) and ocean alkalinity enhancement (OAE; d–f) experiments at 30 days after the beginning of the perturbation simulations. (a) Total dissolved Fe ($[Fe]$), (b) dissolved Fe anomaly ($\Delta[Fe]$), and (c) pCO_2 anomaly for the OIF simulation. (d) Dissolved alkalinity (ALK), (e) dissolved alkalinity anomaly (ΔALK), and (f) pCO_2 anomaly for the OAE simulation. Arrows show the surface current field, while red contours show sea surface dynamic topography, indicating the position of the SAF and the cyclonic eddy. The two boxed regions are used for the regional integration, including a $2^\circ \times 2^\circ$ “single eddy” (solid) region for a smaller patch of water and a $10^\circ \times 5^\circ$ “Subantarctic” region (dash) for a larger domain to evaluate lateral transport and dilution.

simulations deploy dissolved Fe and alkalinity fluxes that are designed to have similar overall impacts on dissolved CO_2 (and thus should result in similar integrated ocean carbon uptake; see Appendix B).

A snapshot of dissolved Fe, alkalinity, and CO_2 at 30 day subsequent to the initiation of iron and alkalinity release is shown in Figure 7. The imposed fluxes are placed in the northern fringe of a cyclonic eddy at the equatorial flank of the Subantarctic Front (SAF) ($139^\circ W$, $48^\circ S$; Figure 7) during January 2009. The summer month is chosen as an optimal season for OIF and OAE due to the relatively warm stratified conditions. Injected alkalinity and iron remain within the surface mixed layer for a relatively longer time. This enables the subsequent air-sea gas exchange to absorb atmospheric CO_2 over a longer period. Furthermore, the biological productivity would be limited by the availability of iron, causing a stronger impact on the biological drawdown in OIF. The impacts of the OIF and OAE experiments are visualized by taking the difference from the baseline simulation. The level of deployment in our simulations is relatively small (corresponding to 700 kg of total dissolved Fe) and resultant perturbations to the background dissolved Fe and alkalinity fields (Figures 7b and 7e) and associated changes in surface ocean pCO_2 (Figures 7c and 7f) are also small and would be challenging to detect by in situ monitoring. Nevertheless, the simulated deployment results in a significant perturbation to the integrated air-sea transfer of CO_2 . The evolution in surface biogeochemical properties and fluxes are evaluated at two scales, including a $2^\circ \times 2^\circ$ “single eddy” (solid line in Figure 3) region for a smaller patch of water and a $10^\circ \times 5^\circ$ “Subantarctic” region (dash line in Figure 3) for a larger domain. By contrasting these two scales, the role of lateral transport and dilution can be evaluated.

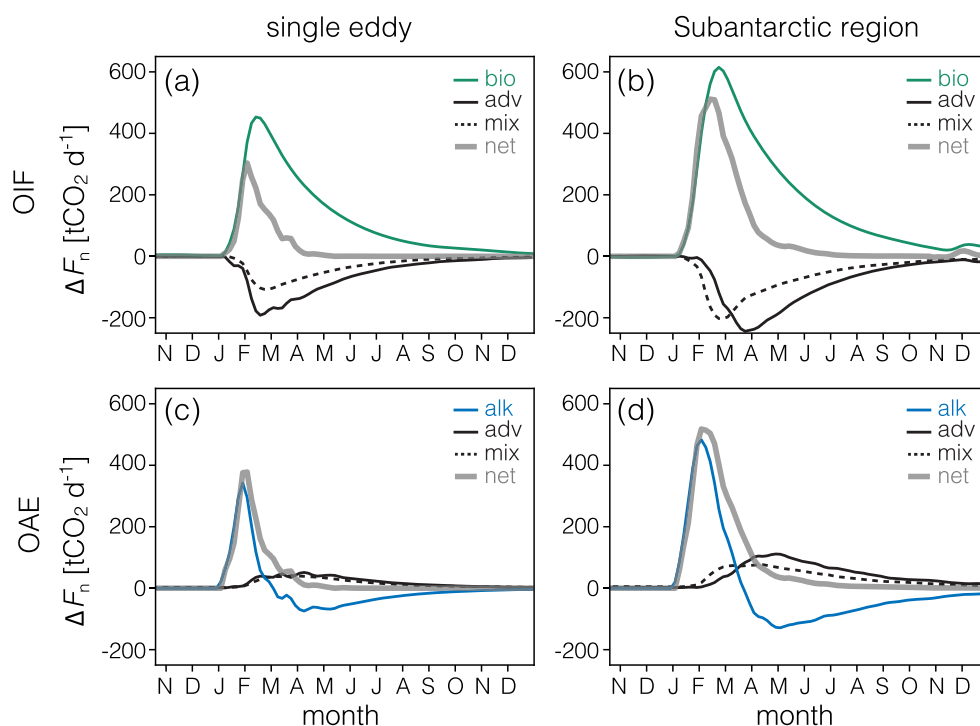


Figure 8. Attribution of carbon flux anomalies for the OIF (a, b) and OAE (c, d) experiments. Carbon flux anomalies (ΔF_n) are calculated as the difference between perturbation and control experiments. In (a, c) anomalies integrated over the “single eddy” region, and in (b, d), carbon flux anomalies are integrated over the larger “Subantarctic” region. Positive values indicate flux into the ocean.

In the Fe fertilization case, the dissolved Fe anomaly is small and relatively short-lived due to rapid consumption by phytoplankton. Anomalies in dissolved Fe and biological carbon fixation are mostly confined to the eddy (Figure 7b) with slight leakage to the outside of the eddy, but the dissolved CO_2 anomaly is longer-lived and emerges significantly afield of the deployment location due to ocean transport (Figure 7c). Increased biological activity causes a localized negative anomaly in dissolved inorganic carbon (C) in near-surface waters. Horizontal turbulent mixing distributes the negative anomaly over a progressively wider surface area, catalyzing the uptake of CO_2 from the atmosphere through air-sea gas transfer. However, vertical turbulent mixing supplies C from the ocean interior, which counteracts the initial transient C gradient and reduces CO_2 uptake efficiency from the atmosphere.

Rapid, eddy-scale re-distribution causes significant dilution of $p\text{CO}_2$ anomalies (~ 1 ppm) but these still drive significant ocean uptake of CO_2 when integrated over the eddy area (solid box, Figure 7)—corresponding to an eddy-wide net air-sea CO_2 flux of up to 300 tonnes of CO_2 per day ($\text{tCO}_2 \text{ d}^{-1}$; Figure 8a) and a total uptake of $\sim 11 \text{ ktCO}_2$ over several months following transient Fe release. The CO_2 anomaly is transported northeastwards of the eddy over the course of several months, while the amplitude of the anomaly attenuates due to physical mixing and air-sea equilibration through gas exchange. When integrated over the larger domain (dashed box, Figure 7) the regional mean $p\text{CO}_2$ perturbation is even smaller (~ 0.1 ppm), but the regional uptake is greater ($\sim 28 \text{ ktCO}_2$), corresponding to an efficiency ratio of $\sim 40 \text{ tCO}_2$ per kgFe. Relatively high sequestration efficiency is likely due to summer stratification and relatively weak vertical turbulent mixing, which minimizes the negative transport feedback on air-sea CO_2 flux. Also, this efficiency estimate does not include the potential negative effects of excess macro-nutrient consumption, which can reduce biological productivity in the downstream region (often referred to as “nutrient robbing”). Thus, this efficiency ratio should be considered as a theoretical upper bound.

The integrated increase in CO_2 uptake in the OAE case is—by design—similar in magnitude to that in OIF. A total of 2.1 Geq is injected into the surface ocean at the same location, and the added alkalinity is rapidly entrained into the cyclonic eddy. A similar eddy-scale dissolved CO_2 anomaly occurs with a resultant air-sea CO_2 flux of $\sim 380 \text{ tCO}_2 \text{ d}^{-1}$, and an integrated ocean CO_2 uptake of $\sim 13 \text{ ktCO}_2$ through the alkalinity pulse at the eddy scale.

Carbon uptake induced by alkalinity release generates a localized positive carbon anomaly in surface waters, resulting in a transport feedback that has an opposite sense relative to that of the iron release experiment. Over several months following the injection, the added alkalinity spreads out beyond the eddy. Integrated regionally, a total uptake of ~ 29 ktCO₂ occurs, corresponding to a regional integrated efficiency ratio of ~ 14 gCO₂ per eq of alkalinity. Once they are transported and diluted across a much wider area in the Subantarctic region, the local anomalies in alkalinity and surface ocean p CO₂ are extremely small.

Again, by design, the overall response of air-sea CO₂ flux to iron and alkalinity release is similar in magnitude between the two experiments. However, the responses of ocean transport to these perturbations are different between the two cases. Our linear ODE framework allows us to quantify the underlying mechanisms for this, and in particular the varying roles played by the changes in physical transport (Figure 8). The addition of iron and alkalinity both alter horizontal and vertical gradients of DIC, which in turn alter the carbon transport divergence. These circulation-driven fluxes can have significant impacts on the evolution of air-sea CO₂ flux. To illustrate this, we perform a deconvolution over two different spatial domains—(a) a single eddy; and (b) the Subantarctic region as shown by the solid and dashed box in Figure 7. The former captures the short-term (<30-day, 10–100 km) localized responses, while the latter captures the diluted response over a wider area and over longer timescales (30–90 days, 100–1,000 km).

For the OIF experiment, the three dominant drivers of the air-sea CO₂ flux are biological carbon uptake (green), advection of C (black solid), and turbulent mixing (black dash). For the OAE experiment, the dominant components are the surface alkalinity changes (blue), advection of C (black solid), and turbulent mixing of C (black dash). All other components make insignificant contributions to the net flux, and the sum of the three components closely approximates the net carbon uptake integrated for each domain (gray).

In the Fe fertilization case, there is a strong and immediate biological response that results in CO₂ uptake from the atmosphere (Figure 7c). However, the enhanced biological carbon fixation creates a local surface minimum in C , leading to flux convergence through advection and turbulent mixing that tends to compensate the loss of C and counteract the impact of an enhanced biological carbon pump. As a result of this transport feedback, the response in net ocean carbon uptake is only a fraction of the spatially integrated biological carbon uptake ($\sim 24\%$ in the single eddy case; Figure 8a). Considering the redistribution of anomalies over a wider area, the integrated net flux over the larger Subantarctic domain is broadly similar (comparing Figures 8a and 8b). However, the net air-sea carbon uptake is again significantly smaller than the biologically driven flux ($\sim 44\%$ in the Subantarctic domain; Figure 8b), highlighting the important role of transport feedback across spatial scales.

In the alkalinity release case, there is an initial increase in net ocean carbon uptake induced by increased surface alkalinity (Figures 8c and 8d). This is followed by the decline of alkalinity-driven carbon flux as the alkalinity pulse decays due to horizontal and vertical mixing ($dAlk/dt$ and the associated f_n term are negative during the spreading phase). The negative overshoot of alkalinity-driven carbon flux occurs due to its slower decay (relative to the injection) in combination with the finite-timescale response of air-sea gas transfer. During the alkalinity addition, increasing alkalinity drives air-to-sea CO₂ uptake (Equation 4), but its potential is not fully realized due to the finite air-sea CO₂ exchange timescale and the mixing away of the surface alkalinity anomaly. When the alkalinity addition ends, physical transport and mixing start to dilute the surface alkalinity, decreasing the local alkalinity, which tends toward sea-to-air CO₂ outgassing. However, the dilution phase usually takes longer than the initial increase, and a negative overshoot occurs due to a more complete air-sea CO₂ equilibration during the dilution phase. However, this negative overshoot does not result in net degassing of CO₂ (Figures 8c and 8d) due to the compensation from the transport of the initial carbon anomaly stored during the alkalinity release phase. The initial alkalinity-driven carbon uptake drives a positive C anomaly in surface waters, the attenuation of which allows just enough carbon uptake tendency to counteract the alkalinity overshoot during the dilution phase. This is not a coincidence—the size of the C anomaly is linked to the magnitude of alkalinity injection, and the attenuation of both carbon and alkalinity anomalies is driven by the same circulation field. The temporal evolution is generally similar between the small and large domains (Figures 8c and 8d), again suggesting the importance of vertical transport across spatial scales.

6. Discussion

Attribution of simulated CO₂ fluxes to different processes generally requires performing multiple sensitivity simulations with one factor varied at a time and comparing the resulting CO₂ fluxes to a background reference

condition. Recent theoretical advances enable the attribution of surface ocean $p\text{CO}_2$ tendencies for mean seasonal cycles (Ayers & Lozier, 2012) and for climatological air-sea CO_2 fluxes (Lauderdale et al., 2016). Building on these studies, we present a new approach that can deconvolve air-sea CO_2 fluxes into different mechanistic components in a time-dependent manner, including natural variability and imposed mCDR perturbations. Our approach requires only a single simulation to record all the f_n terms, with the attribution to different factors calculated via the linear ODE.

Using idealized ocean CDR experiments and our new analytical framework, we demonstrate that correctly understanding and quantifying the response of air-sea carbon exchange to surface ocean perturbation requires the integration of direct forcings, such as changes to biological carbon cycling or shifts in surface alkalinity, with indirect responses caused by changing tracer gradients and physical transport. For example, the direct effect of iron addition to the surface ocean will be enhanced biological carbon drawdown, but this biological drawdown alters local carbon gradients in both horizontal and vertical directions, leading to an indirect carbon tendency driven by ocean carbon transport. Our results show that these indirect effects can contribute significantly to carbon uptake as a positive or negative feedback depending on the specific style of perturbation and background ocean state.

Another example is the direct and indirect effects of alkalinity addition. Increased alkalinity directly affects air-sea CO_2 flux through changes in surface water chemistry. However, it also alters the spatial gradients and the carbon transport, which causes an indirect transport effect. The strength of these indirect effects depends on local mixing and circulation dynamics, which may affect the efficiency of the mCDR approach at different locations and times throughout an annual cycle. Importantly, it is impossible to separate the direct and indirect effects by only comparing a sensitivity experiment to a control, while the autoregression model provides a theoretical framework to deconvolve these effects from a single simulation pair. This framework may help to achieve more confident and specific attribution of background carbon fluxes in Earth's oceans, providing scope for more confident assessment of anthropogenic environmental impacts and natural carbon cycle dynamics across a wide range of surface ocean environments. Another fruitful future direction is to apply this attribution framework to recently emerging biogeochemical ocean state estimates (e.g., Carroll et al., 2020; Verdy & Mazloff, 2017). Our framework can also serve as a tool for predicting and quantifying the impact of anthropogenic modification of surface ocean chemistry on air-sea CO_2 fluxes, making it a potentially powerful tool for designing and optimizing field trials, developing robust measurement and verification frameworks, and augmenting technoeconomic assessment across a range of ocean CDR strategies.

Appendix A: Derivation of the Theory

The time derivative of the gas exchange formula (Equation 3) yields four terms that explain the temporal change of air-sea CO_2 flux (F), including the rate of change in gas exchange coefficient (G^*), solubility (K_H), atmospheric partial pressure ($p\text{CO}_2^{\text{atm}}$), and surface ocean $[\text{CO}_2]$ as follows

$$\partial F / \partial t = \dot{G}^* \{ K_H p\text{CO}_2^{\text{atm}} - [\text{CO}_2] \} + G^* \dot{K}_H p\text{CO}_2^{\text{atm}} + G^* K_H p\dot{\text{CO}}_2^{\text{atm}} - G^* [\dot{\text{CO}}_2] \quad (\text{A1})$$

where the dot is the time derivative. Then, the last term involving surface ocean CO_2 can be linked to the surface ocean budget of dissolved inorganic carbon (C , Equation 1) via the use of carbonate chemistry (Equation 2).

$$\frac{\partial [\text{CO}_2]}{\partial t} = \frac{\partial [\text{CO}_2]}{\partial \text{DIC}} \frac{\partial \text{DIC}}{\partial t} = \frac{\partial [\text{CO}_2]}{\partial \text{DIC}} \left\{ -\nabla \cdot uC + \nabla \cdot K \nabla C - B + \frac{C}{h} (E - P) + \frac{F}{h} \right\} \quad (\text{A2})$$

Combining Equations A1 and A2, we eliminate the time derivative of $[\text{CO}_2]$. The last term in Equation A2 indicates the negative feedback from the air-sea gas exchange. We rearrange terms such that we combine terms that depend primarily on temperature in carbonate chemistry and solubility. Similarly, we combine terms that depend on salinity in carbonate chemistry and the net evaporation minus precipitation. We then arrive at the expression shown in Equation 4.

Appendix B: Design of Iron and Alkalinity Release Experiments

In the ocean iron fertilization (OIF) simulation, 700 kg of dissolved iron is injected over five grid cells (570 km²) for a 1-month period during mid-summer (January), when the background surface dissolved iron concentrations are relatively low. Our objective is to estimate the amount of alkalinity addition required to induce a similar impact on the surface ocean *p*CO₂ in our ocean alkalinity enhancement (OAE) simulation, and thus to roughly control for the overall degree of ocean carbon uptake while examining differences in carbon flux partitioning between methods. The flux of iron is calculated as

$$\begin{aligned} 700 \text{ kgFe} / 570 \text{ km}^2 / 1 \text{ month} &= 1.22 \text{ kgFe} / \text{km}^2 / \text{month} = 1.22 \text{ mgFe} / \text{m}^2 / \text{month} \\ &= 0.022 \text{ mmolFe m}^{-2} \text{ month}^{-1} \end{aligned} \quad (\text{B1})$$

It is possible to stoichiometrically convert this amount of iron to organic carbon assuming a certain utilization efficiency. For example, one may assume that added iron is utilized at 50% efficiency to increase net community production beyond the background value. In the Southern Ocean, we expect Fe to be the limiting nutrient, and we assume that organic ligand abundance is sufficient to retain all added Fe, so we set a relatively high utilization ratio. This additional production of organic carbon equates to a loss of dissolved inorganic carbon (*C*) from surface waters, which is translated into a decrease in surface water *p*CO₂.

The ratio of iron to phosphorus in the model (Fe:P) is taken from Galbraith et al. (2010), which uses a Monod function to reduce the Fe:P ratio as ambient dissolved Fe availability decreases. Based on an ambient dissolved Fe level of 0.1 nM, the Fe:P molar ratio is 0.4×10^{-3} . Given a P:C ratio of 110,

$$\begin{aligned} 0.022 \text{ mmolFe} / \text{m}^2 / \text{month} \times 2.5 \text{ molP} / \text{mmolFe} \times 110 \text{ molC} / \text{molP} \times 0.5 \\ = 3.1 \text{ molC m}^{-2} \text{ month}^{-1}. \end{aligned} \quad (\text{B2})$$

This means that 3.1 molC will be removed per unit area over the 1-month period. Considering a surface layer of 100 m thickness, this translates to 31 μmolC kg⁻¹ of carbon loss. We note that this number is probably unrealistic since ocean currents and turbulent mixing will immediately spread the injected iron over a much wider area. We also assume that the degree of dilution is the same between iron and alkalinity, which is probably not entirely accurate due to different spatial gradients. The assumed 50% iron utilization efficiency may also be unrealistic. However, with these uncertainties in mind, our goal here is to roughly estimate the amount of alkalinity needed to induce a similar amount of carbon removal—for example, a perturbation of −31 μmolC kg⁻¹ in surface waters.

To first order, the required amount of alkalinity change (ΔAlk) for a given *C* perturbation (Δ*C*) can be estimated as follows:

$$\Delta \text{Alk} = 1.23 \times \Delta C = 1.23 \times 31 \text{ } \mu\text{molC} / \text{kg} = 37 \text{ } \mu\text{eq kg}^{-1} \quad (\text{B3})$$

Considering a surface layer of 100 m thickness, this translates to 3.7 eq m⁻² month⁻¹ of alkalinity injection over a 1-month period. The total amount of alkalinity required is therefore:

$$3.7 \text{ eq} / \text{m}^2 / \text{month} \times 570 \text{ km}^2 \times 1 \text{ month} = 3.7 \text{ eq} / \text{m}^2 \times 570 \times 10^6 \text{ m}^2 = 2.1 \text{ Geq.} \quad (\text{B4})$$

This is the total amount of estimated alkalinity required to induce a CO₂ drawdown equivalent to the effects of a 700 kg Fe release. The imposed fluxes are placed in the northern fringe of a cyclonic eddy at the equatorial flank of the Subantarctic Front (SAF) 139°W, 48°S.

Data Availability Statement

The Jupyter Notebook to execute the stochastic box model in Section 3 of the paper is hosted at the Github repository and the results can be replicated on a cloud server (Ito, 2024). Modifications to the Massachusetts Institute of Technology General Circulation Model source code and scripts and instructions to reproduce input files for the regional Southern Ocean model simulations are available as the Regional Southern Ocean package (Ito & Jersild, 2020) and are documented in detail in Ito (2022).

Acknowledgments

We are thankful for the funding support from U.S. Department of Energy, DE-SC0021300 and DE-SC0024709.

References

- Ayers, J. M., & Lozier, M. S. (2012). Unraveling dynamical controls on the North Pacific carbon sink. *Journal of Geophysical Research*, *117*(C1). <https://doi.org/10.1029/2011JC007368>
- Boyd, P. W., Watson, A. J., Law, C. S., Abraham, E. R., Trull, T., Murdoch, R., et al. (2000). A mesoscale phytoplankton bloom in the polar Southern Ocean stimulated by iron fertilization. *Nature*, *407*(6805), 695–702. Article. <Go to ISI>://WOS:000089773900031. <https://doi.org/10.1038/35037500>
- Broecker, W. S., & Peng, T. H. (1974). Gas exchange rates between air and sea. *Tellus*, *26*(1–2), 21–35. <https://doi.org/10.1111/j.2153-3490.1974.tb01948.x>
- Buesseler, K. O., Andrews, J. E., Pike, S. M., & Charette, M. A. (2004). The effects of iron fertilization on carbon sequestration in the Southern Ocean. *Science*, *304*(5669), 414–417. <https://doi.org/10.1126/science.1086895>
- Cai, W.-J., Xu, Y.-Y., Feely, R. A., Wanninkhof, R., Jönsson, B., Alin, S. R., et al. (2020). Controls on surface water carbonate chemistry along North American ocean margins. *Nature Communications*, *11*(1), 2691. <https://doi.org/10.1038/s41467-020-16530-z>
- Carroll, D., Menemenlis, D., Adkins, J. F., Bowman, K. W., Brix, H., Dutkiewicz, S., et al. (2020). The ECCO-Darwin data-assimilative global ocean biogeochemistry model: Estimates of seasonal to multidecadal surface ocean $p\text{CO}_2$ and air-sea CO_2 flux. *Journal of Advances in Modeling Earth Systems*, *12*(10), e2019MS001888. <https://doi.org/10.1029/2019MS001888>
- Di Lorenzo, E., & Ohman, M. D. (2013). A double-integration hypothesis to explain ocean ecosystem response to climate forcing. *Proceedings of the National Academy of Sciences of the United States of America*, *110*(7), 2496–2499. <https://doi.org/10.1073/pnas.1218022110>
- Dutkiewicz, S., Hickman, A. E., Jahn, O., Gregg, W. W., Mouw, C. B., & Follows, M. J. (2015). Capturing optically important constituents and properties in a marine biogeochemical and ecosystem model. *Biogeosciences*, *12*(14), 4447–4481. <https://doi.org/10.5194/bg-12-4447-2015>
- Dutkiewicz, S., Ward, B. A., Scott, J. R., & Follows, M. J. (2014). Understanding predicted shifts in diazotroph biogeography using resource competition theory. *Biogeosciences*, *11*(19), 5445–5461. <https://doi.org/10.5194/bg-11-5445-2014>
- Eisaman, M. D. (2020). Negative emissions technologies: The tradeoffs of air-capture economics. *Joule*, *4*(3), 516–520. <https://doi.org/10.1016/j.joule.2020.02.007>
- Fassbender, A. J., Rodgers, K. B., Palevsky, H. I., & Sabine, C. L. (2018). Seasonal asymmetry in the evolution of surface ocean $p\text{CO}_2$ and pH thermodynamic drivers and the influence on sea-air CO_2 flux. *Global Biogeochemical Cycles*, *32*(10), 1476–1497. <https://doi.org/10.1029/2017gb005855>
- Fay, A. R., Gregor, L., Landschützer, P., McKinley, G. A., Gruber, N., Gehlen, M., et al. (2021). SeaFlux: Harmonization of air–sea CO_2 fluxes from surface $p\text{CO}_2$ data products using a standardized approach. *Earth System Science Data*, *13*(10), 4693–4710. <https://doi.org/10.5194/essd-13-4693-2021>
- Ferderer, A., Chase, Z., Kennedy, F., Schulz, K. G., & Bach, L. T. (2022). Assessing the influence of ocean alkalinity enhancement on a coastal phytoplankton community. *Biogeosciences*, *19*(23), 5375–5399. <https://doi.org/10.5194/bg-19-5375-2022>
- Follows, M., & Williams, R. G. (2004). Mechanisms controlling the air-sea flux of CO_2 in the North Atlantic. In M. Follows & T. Oguz (Eds.), *The ocean carbon cycle and climate*, NATO Science Series (Vol. 40, pp. 217–249). Springer. https://doi.org/10.1007/978-1-4020-2087-2_7
- Friedlingstein, P., Jones, M. W., O’Sullivan, M., Andrew, R. M., Bakker, D. C. E., Hauck, J., et al. (2022). Global carbon budget 2021. *Earth System Science Data*, *14*(4), 1917–2005. <https://doi.org/10.5194/essd-14-1917-2022>
- Galbraith, E. D., Gnanadesikan, A., Dunne, J. P., & Hiscock, M. R. (2010). Regional impacts of iron-light colimitation in a global biogeochemical model. *Biogeosciences*, *7*(3), 1043–1064. <https://doi.org/10.5194/bg-7-1043-2010>
- Gruber, N., Bakker, D. C. E., DeVries, T., Gregor, L., Hauck, J., Landschützer, P., et al. (2023). Trends and variability in the ocean carbon sink. *Nature Reviews Earth & Environment*, *4*(2), 119–134. <https://doi.org/10.1038/s43017-022-00381-x>
- Gruber, N., Clement, D., Carter, B. R., Feely, R. A., van Hueven, S., Hoppema, M., et al. (2019). The oceanic sink for anthropogenic CO_2 from 1994 to 2007. *Science*, *363*(6432), 1193–1199. <https://doi.org/10.1126/science.aau5153>
- Hamme, R. C., & Emerson, S. R. (2002). Mechanisms controlling the global oceanic distribution of the inert gases argon, nitrogen and neon. *Geophysical Research Letters*, *29*(23), 2120. <https://doi.org/10.1029/2002GL015273>
- Hasselmann, K. (1976). Stochastic climate models Part I. Theory. *Tellus*, *28*(6), 473–485. <https://doi.org/10.3402/tellusa.v28i6.11316>
- Hooss, G., Voss, R., Hasselmann, K., Maier-Reimer, E., & Joos, F. (2001). A nonlinear impulse response model of the coupled carbon cycle-climate system (NICCS). *Climate Dynamics*, *18*(3), 189–202. <https://doi.org/10.1007/s003820100170>
- Humphreys, M. P., Lewis, E. R., Sharp, J. D., & Pierrot, D. (2022). PyCO2SYS v1.8: Marine carbonate system calculations in Python. *Geoscientific Model Development*, *15*(1), 15–43. <https://doi.org/10.5194/gmd-15-15-2022>
- Ito, T. (2022). Development of the regional carbon cycle model in the central Pacific sector of the Southern Ocean. *Journal of Advances in Modeling Earth Systems*, *14*(6), e2021MS002757. <https://doi.org/10.1029/2021MS002757>
- Ito, T. (2024). takaito1/car1: Carbon flux AR-1 (CAR1) model (v1.0) [Software]. *Zenodo*. <https://doi.org/10.5281/zenodo.14564221>
- Ito, T., & Jersild, A. (2020). eas2655-taka/RSO: Regional Southern Ocean (v3.0) [Software]. *Zenodo*. <https://doi.org/10.5281/zenodo.5833949>
- Jersild, A., & Ito, T. (2020). Physical and biological controls of the Drake Passage $p\text{CO}_2$ variability. *Global Biogeochemical Cycles*, *34*(9), e2020GB006644. <https://doi.org/10.1029/2020GB006644>
- Jones, D. C., Ito, T., Takano, Y., & Hsu, W.-C. (2014). Spatial and seasonal variability of the air-sea equilibration timescale of carbon dioxide. *Global Biogeochemical Cycles*, *28*(11), 1163A–1178. <https://doi.org/10.1002/2014GB004813>
- Joos, F., & Bruno, M. (1996). Pulse response functions are cost-efficient tools to model the link between carbon emissions, atmospheric CO_2 and global warming. *Physics and Chemistry of the Earth*, *21*(5), 471–476. [https://doi.org/10.1016/s0079-1946\(97\)81144-5](https://doi.org/10.1016/s0079-1946(97)81144-5)
- Large, W. G., McWilliams, J. C., & Doney, S. C. (1994). Oceanic vertical mixing: A review and a model with a nonlocal boundary layer parameterization. *Reviews of Geophysics*, *32*(4), 363–403. <https://doi.org/10.1029/94RG01872>
- Lauderdale, J. M., Dutkiewicz, S., Williams, R. G., & Follows, M. J. (2016). Quantifying the drivers of ocean-atmosphere CO_2 fluxes. *Global Biogeochemical Cycles*, *30*(7), 983A–999. <https://doi.org/10.1002/2016GB005400>
- Lebling, K., Northrop, E., McCormick, C., & Bridgwater, E. (2022). Towards responsible and informed ocean-based carbon dioxide removal: Research and governance priorities. Washington, DC.
- Lovenduski, N. S., Gruber, N., Doney, S. C., & Lima, I. D. (2007). Enhanced CO_2 outgassing in the Southern Ocean from a positive phase of the Southern Annular Mode. *Global Biogeochemical Cycles*, *21*(2), GB2026. <https://doi.org/10.1029/2006GB002900>
- Marshall, J., Adcroft, A., Hill, C., Perelman, L., & Heisey, C. (1997). A finite-volume, incompressible Navier Stokes model for studies of the ocean on parallel computers. *Journal of Geophysical Research*, *102*(C3), 5753–5766. <https://doi.org/10.1029/96JC02775>
- Marshall, J., Hill, C., Perelman, L., & Adcroft, A. (1997). Hydrostatic, quasi-hydrostatic, and nonhydrostatic ocean modeling. *Journal of Geophysical Research*, *102*(C3), 5733–5752. <https://doi.org/10.1029/96JC02776>

- McKinley, G. A., Fay, A. R., Lovenduski, N. S., & Pilcher, D. J. (2017). Natural variability and anthropogenic trends in the ocean carbon sink. *Annual Review of Marine Science*, 9(1), 125–150. <https://doi.org/10.1146/annurev-marine-010816-060529>
- National Academies of Sciences, E., and Medicine. (2021). A research strategy for ocean-based carbon dioxide removal and sequestration. Washington, DC.
- Rau, G. H. (2009). Electrochemical CO₂ capture and storage with hydrogen generation. *Energy Procedia*, 1, 823–828. <https://doi.org/10.1016/j.egypro.2009.01.109>
- Redfield, A. C., Ketchum, B. H., & Richards, F. A. (1963). The influence of organisms on the composition of the sea water. In M. N. Hill (Ed.), *The Sea* (Vol. 2, pp. 26–77). Interscience Publishers.
- Sarmiento, J. L., & Gruber, N. (2006). *Ocean biogeochemical dynamics*. Princeton University Press. <https://doi.org/10.2307/j.ctt3fgxqx>
- Takahashi, T., Olafsson, J., Goddard, J. G., Chipman, D. W., & Sutherland, S. C. (1993). Seasonal variation of CO₂ and nutrients in the high-latitude surface oceans: A comparative study. *Global Biogeochemical Cycles*, 7(4), 843–878. <https://doi.org/10.1029/93gb02263>
- Takahashi, T., Sutherland, S. C., Sweeney, C., Poisson, A., Metz, N., Tilbrook, B., et al. (2002). Global sea-air CO₂ flux based on climatological surface ocean pCO₂, and seasonal biological and temperature effects. *Deep-Sea Research II*, 49(9–10), 1601–1622. [https://doi.org/10.1016/s0967-0645\(02\)00003-6](https://doi.org/10.1016/s0967-0645(02)00003-6)
- Verdy, A., & Mazloff, M. R. (2017). A data assimilating model for estimating Southern Ocean biogeochemistry. *Journal of Geophysical Research: Oceans*, 122(9), 6968–6988. <https://doi.org/10.1002/2016JC012650>
- Wang, X., Christian, J. R., Murtugudde, R., & Busalacchi, A. J. (2006). Spatial and temporal variability of the surface water pCO₂ and air-sea CO₂ flux in the equatorial Pacific during 1980–2003: A basin-scale carbon cycle model. *Journal of Geophysical Research*, 111(C7), C07S04. <https://doi.org/10.1029/2005jc002972>
- Wanninkhof, R. (2014). Relationship between wind speed and gas exchange over the ocean revisited. *Limnology and Oceanography: Methods*, 12(6), 351–362. Article. <Go to ISI>://WOS:000339548800002. <https://doi.org/10.4319/lom.2014.12.351>
- Yankovsky, E., Zhou, M., Tyka, M., Bachman, S., Ho, D., Karspeck, A., & Long, M. (2024). Impulse response functions as a framework for quantifying ocean-based carbon dioxide removal. *EGU Sphere*, 2024, 1–26.
- Yuan, G.-C., Lozier, M. S., Pratt, L. J., Jones, C. K. R. T., & Helfrich, K. R. (2004). Estimating the predictability of an ocean time series using linear and nonlinear methods. *Journal of Geophysical Research*, 109(C8), C08002. <https://doi.org/10.1029/2003jc002148>